# Development of a digital twin of a tablet that mimics a real solid dosage form: Differences in the dissolution profile in conventional mini-USP II and a biorelevant colon model

M. Schütt [a], K. Stamatopoulos [a,b], H.K. Batchelor [c], M.J.H. Simmons [a], A. Alexiadis [a,*]

[a] *School of Chemical Engineering, University of Birmingham, Edgbaston, Birmingham B15 2TT, United Kingdom*

[b] *Biopharmaceutics, Pharmaceutical Development, PDS, MST, RD Platform Technology & Science, GSK, David Jack Centre, Park Road, Ware, Hertfordshire SG12 0DP, United Kingdom*

[c] *Strathclyde Institute of Pharmacy and Biomedical Sciences, University of Strathclyde, 161 Cathedral Street, Glasgow G4 0RE, United Kingdom*

ABSTRACT

The performance of colon-targeted solid dosage forms is commonly assessed using standardised pharmacopeial dissolution apparatuses like the USP II or the miniaturised replica, the mini-USP II. However, these fail to replicate the hydrodynamics and shear stresses in the colonic environment, which is crucial for the tablet's drug release process. In this work, computer simulations are used to create a digital twin of a dissolution apparatus and to develop a method to create a digital twin of a tablet that behaves realistically. These models are used to investigate the drug release profiles and shear rates acting on a tablet at different paddle speeds in the mini-USP II and biorelevant colon models to understand how the mini-USP II can be operated to achieve more realistic (i.e., *in vivo*) hydrodynamic conditions.

The behaviour of the tablet and the motility patterns used in the simulations are derived from experimental and in vivo data, respectively, to obtain profound insights into the tablet's disintegration/drug release processes. We recommend an "on-off" operating mode in the mini-USP II to generate shear rate peaks, which would better reflect the *in vivo* conditions of the human colon instead of constant paddle speed.

## 1. Introduction

The performance of a drug formulation is commonly accessed using United States Pharmacopeia (USP) dissolution apparatus. Besides drug performance analysis, this in vitro drug testing tool is also used in product development and quality control (Abrahamsson et al., 2005; Stamatopoulos et al., 2015). The USP dissolution apparatus are simplified *in vitro* models also used to replicate the complex *in vivo* conditions in the gastrointestinal tract that significantly control the disintegration/dissolution process of a solid dosage form (e.g., shear stresses evoked by wall motion) (Schütt et al., 2021). The USP II is the commonly most used USP dissolution apparatus for evaluating solid oral dosage forms (Stamatopoulos et al., 2015). The USP II is a container equipped with an agitator (paddle) and a fluid volume capacity of approximately one litre (Stamatopoulos et al., 2015). The most commonly used volumes are 500 and 900 mL. A miniaturised version of the USP II, the mini-USP II has received more attention in recent years

because this dissolution test device requires significantly less material mass than its larger counterpart (i.e., fluid volume of approximately 100 mL) (Stamatopoulos et al., 2015; Klein and Shah, 2008). This is of particular interest when biorelevant media or cost-intensive samples are used (Klein and Shah, 2008).

The dissolution profile of a solid dosage is of paramount importance in the development and optimisation of new formulations. Furthermore, the dissolution profile serves as a basis for physiologically based pharmacokinetic models (PBPK) to predict the absorption of drugs based on human physiology and their chemical properties (Stamatopoulos, 2022).

Investigations of the USP II showed that the shear rates in this dissolution apparatus depend on the paddle speed used (Hopgood et al., 2018). These results can also be transferred to the mini-USP II (Klein and Shah, 2008). However, Schütt et al. (2021) showed in a computational model of the proximal colon and a modelled tablet that the shear stresses acting on the tablet surface and thus influencing the tablet drug release
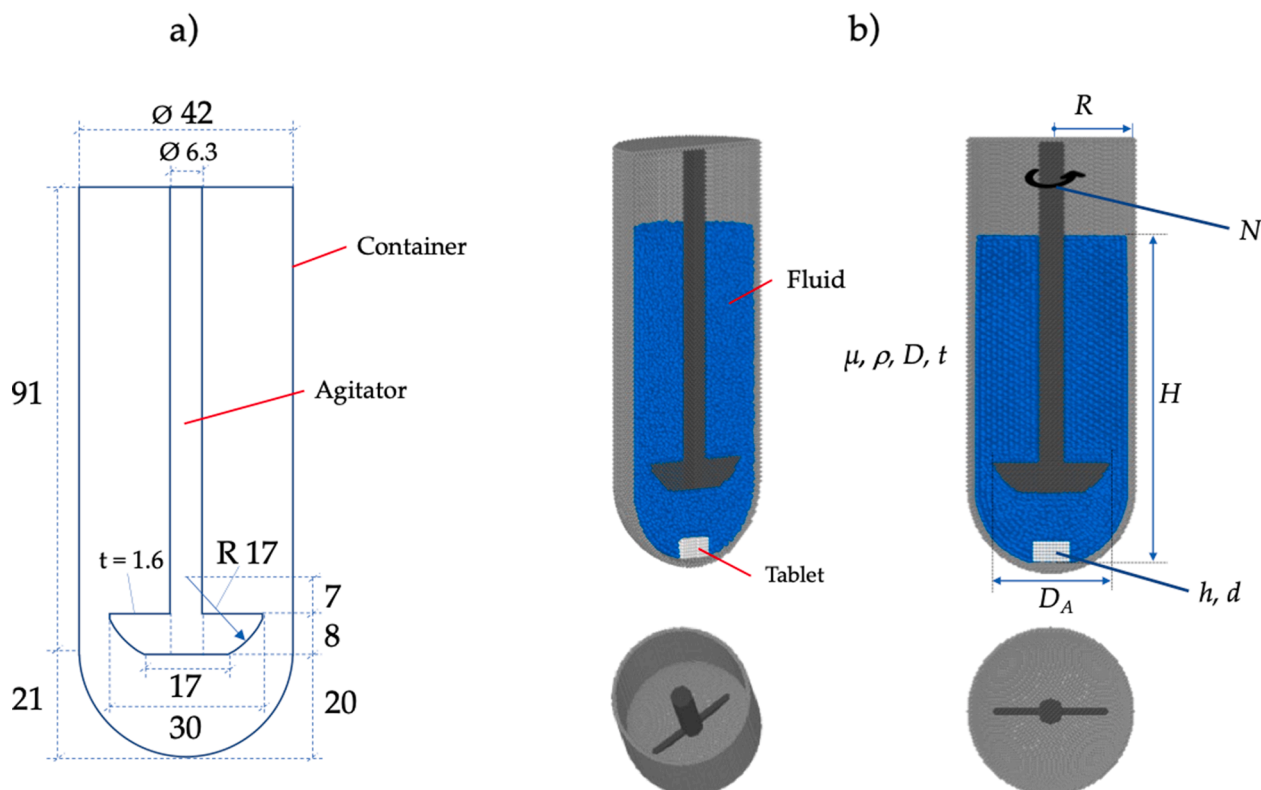
**Fig. 1.** Schematic representation of the mini-USP II with the dimensions used in Stamatopoulos et al. (2015) (a) and the computational model (b) including the variables for the dimensional analysis (Section 2.2.2).

process mainly depend on the colonic motility and the forces are dynamic.

In this study, we develop a method to model create a digital twin of a tablet with the same disintegration/dissolution behaviour as a real tablet. Additionally, we create a digital twin of the mini-USP II dissolution apparatus and validate the hydrodynamic conditions with experimental and computational data from Stamatopoulos et al. (2015) and Wang and Armenante (2016). Then, we use experimental dissolution data of a tablet from Stamatopoulos et al. (2015) and model a tablet that behaves similarly in the modelled mini-USP II. Finally, this tablet is used in a biorelevant computational model of the proximal colon replicating in vivo motility patterns to evaluate the difference in drug release profile in the simplified in vitro model and the more realistic colon model. The motility patterns used in the colon models (i.e., called 'PEG' and Maltose') are reproduced from Schütt et al. (2021).

## 2. Methodology

### 2.1. Modelling approach

This study uses a simulation technique called Discrete Multiphysics (DMP) (Alexiadis, 2015, 2014). DMP is a mesh-free technique that uses computational particles instead of computational grids and has been successfully used to model human organs: Ariane et al. (2017a, 2018a, 2018b, 2017b), Baksamawi et al. (2021), Mohammed et al. (2020, 2021), Alexiadis (2015b, 2015a, 2019), Alexiadis et al. (2017), and Schütt et al. (2021, 2022, 2020). It couples particle-based methods such as Smoothed Particle Hydrodynamics (SPH), Lattice Spring Model (LSM), and Discrete Element Method (DEM) and Peridynamics (Sanfilipo et al., 2021). In particular, the model in this study couples SPH and LSM. In the mini-USP II model and the colon models, SPH is used to model the fluid, while the colon models also account for LSM to model the colon's membrane. The reader can refer to Refs. Alexiadis (2015b,

2015a), Ref. Liu and Liu (2003), and Refs. Kot (2021), Kot et al. (2015), Pazdniakou and Adler (2012) for a general overview of the DMP, SPH and LSM theory, respectively. The solid dosage form dissolution is modelled similarly to the methodology discussed in Schütt et al. (2021).

### 2.2. Mini-USP II model

#### 2.2.1. Geometry container and impeller

The mini-USP II dissolution apparatus (also called small volume dissolution apparatus) consists of a cylindrical container with a hemispherical bottom. The agitator, also called paddle, rotates at a specified speed and accelerates the fluid in the container. In this study, the rotational speed of the mini-USP II is 50 rpm as in Stamatopoulos et al. (2015). A schematic representation of the mini-USP II (100 mL capacity) and the computational model is given in Fig. 1(a) and Fig. 1(b), respectively.

The following model details refer only to the mini-USP II model, which replicates the experimental apparatus of Stamatopoulos et al. (2015). Data from literature (Wang and Armenante, 2016) are used for validation of the model velocity. For validation of the tablet, drug release profile data from Stamatopoulos et al. (2015) are used.

The dimensions of the mini-USP II dissolution apparatus used in Stamatopoulos et al. (2015) and in Wang and Armenante (2016) differ slightly from each other. Therefore, to validate the velocity profile inside the container against experimental data from Wang and Armenante (2016), the dimensions of the model are adjusted (i.e., the paddle clearance, the container diameter, and the diameter of the agitator shaft, see Section 3.1) and the results are compared.

The mini-USP II model has a total height of $1.12 \times 10^{-1}$ m, a diameter of $0.42 \times 10^{-1}$ m and a paddle diameter of $0.30 \times 10^{-1}$ m with a total capacity of 100 mL. Further details are given in Fig. 1(a).

The container walls are built with 69,154 stationary SPH particles. The agitator or paddle is composed of 13,039 SPH particles building a

**Table 1**

mini-USP II parameters.

| Parameter (mini-USP II) | Value |
| --- | --- |
| **SPH** | |
| Number of SPH particles (container) | 69,154 |
| Number of SPH particles (agitator) | 13,039 |
| Mass of each particle $m_C$ | $2.55 \times 10^{-7}$ kg |
| Mass of each particle $m_A$ | $2.40 \times 10^{-7}$ kg |

**Table 2**

Variables for the dimensional analysis.

| | Variable | Unit | Description |
| --- | --- | --- | --- |
| (1) | $t$ | s | Dissolution time |
| (2) | $N$ | $s^{-1}$ | Agitator rotational speed |
| (3) | $h$ | m | Tablet thickness |
| (4) | $d$ | m | Tablet diameter |
| (5) | $\mu$ | $kg\,m^{-1}\,s^{-1}$ | Dynamic viscosity of the fluid |
| (6) | $\rho$ | $kg\,m^{-3}$ | Density of the fluid |
| (7) | $D$ | $m^2\,s^{-1}$ | Diffusion coefficient |
| (8) | $D_A$ | m | Paddle diameter |
| (9) | $H$ | m | Height of the fluid in container |
| (10) | $R$ | m | Radius of the container |

**Table 3**

Dimensionless variables for the dimensional analysis.

| $\Pi_1 = \dfrac{D\,t}{H^2}$ | $\Pi_2 = \dfrac{H^2\,N}{D}$ | $\Pi_3 = \dfrac{h}{H}$ | $\Pi_3 = \dfrac{d}{H}$ |
| --- | --- | --- | --- |
| $\Pi_5 = \dfrac{D_A}{H}$ | $\Pi_6 = \dfrac{R}{H}$ | $\Pi_7 = \dfrac{\mu}{D\,\rho}$ | |

rigid body that rotates at a constant speed of 50 rpm around its longitudinal axis. Further details of the mini-USP II model are given in Table 1.

### 2.2.2. Dimensional analysis

From Buckingham's π-theorem, physically significant equations with $n$ physical variables can be rephrased in terms of several $p = n - k$ dimensionless parameters $\Pi_1, \Pi_2, \ldots, \Pi_p$, where $k$ is the number of physical dimensions involved.

For the case analysed, the results can be expressed as a mathematical function $f$ of the type

$$f(t,\ N,\ h,\ d,\ \mu, \rho, D, D_A, H, R) = 0, \tag{1}$$

where all the variables and their physical units are represented in

Table 2. The listed variables are shown in Fig. 1(b). With the ten variables listed in Table 2, and three units (kg, s, m), Eq. (1) can be rewritten based on seven dimensionless parameters:

$$\varphi(\Pi_1, \ldots, \Pi_7) = 0, \tag{2}$$

The ten dimensional variables are combined into seven dimensionless parameters. One possible way is shown in Table 3.

From the dimensionless $\Pi_1$, we can see that the dimensionless time is inversely proportional to the diffusivity if the height of the fluid in the container is constant (i.e., fluid volume). This result will be used later on (see Section 2.5.2).

### 2.3. Colon model

#### 2.3.1. Geometry, membrane, fluid, and colonic motility

The models used in this study are similar to the 'Stimulant PEG' and 'Stimulant Maltose' represented in Schütt et al. (2021). Both are enlarged models of the human ascending colon (i.e., the length of the colon model is three times the length of the real ascending colon). The model has the form of a cylindrical body with a total length of $6.0 \times 10^{-1}$ m and an inner diameter of $4.0 \times 10^{-2}$ m. The membrane of the models is constricted at regular intervals, representing the colon *haustra*. The models are built with closed ends to ensure no fluid can exit the tube. The closed ends result in a back pressure when the fluid flow reaches the end of the tube. In vivo observations showed that most waves propagate only over a short distance in the proximal colon and usually terminate before the *hepatic flexure*, a sharp bend between the ascending and the transverse colon, creating backflow/back pressure (Bampton et al., 2000; Dinning et al., 2008).

The membrane is composed of 2500 LSM particles and modelled similarly to Schütt et al. (2020). These particles are tied to their initial position with a Hookean spring so that the membrane particles return to their initial position after activation (i.e., contraction or relaxation). This spring also ensures that the model is fixed in the domain during the simulation. The adjacent membrane particles are connected with an additional Hookean force to obtain an elastic membrane. The created lattice structure replicates, therefore, the properties of an elastic solid (Kot et al., 2015). The motility of the colon is achieved by applying a radial force to the particles representing the membrane in a specific pattern. Fig. 2 shows a section of the colon model.

The Hookean forces are calculated using Hooke's law:

$$F_{ij} = k(r_{ij} - r_0), \tag{3}$$

where $F_{ij}$ is the resulting spring force between particle $i$ and $j$. $k$ is the Hookean constant, and $r_{ij}$ represents the current distance between
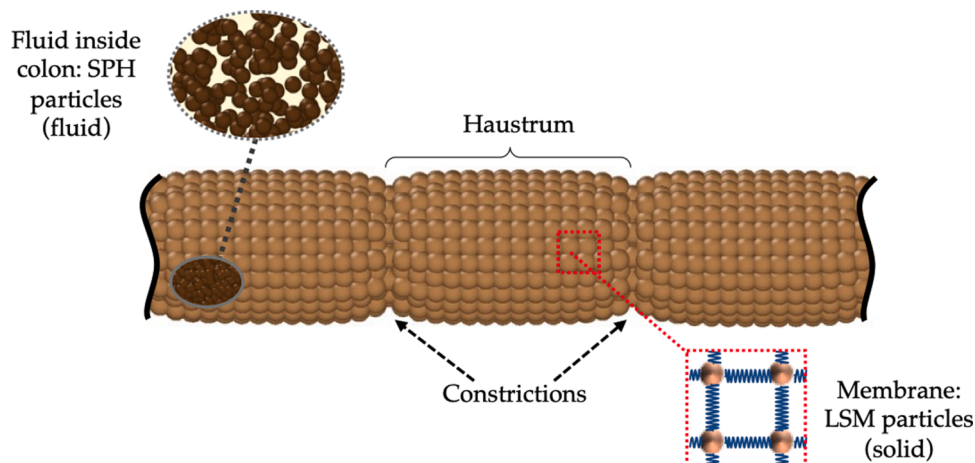


**Fig. 2.** Representation of the colon model showing the construction of the membrane, the constrictions of the membrane building the haustrum, and the SPH particles representing the fluid inside the colon.

**Table 4**
Colon membrane parameters.

| Parameter Membrane (Colon) | Value |
|---|---|
| **SPH** | |
| Number of SPH particles (1 layer) | 2500 |
| Mass of each particle $m_{M,0}$ | $3.89 \times 10^{-4}$ kg |
| **LSM** | |
| Hookean coefficient (bonds) $k_{M,b}$ | 0.2 J $m^{-2}$ |
| Hookean coefficient (position anchor) $k_{M,p}$ | 0.012 J $m^{-2}$ |
| Viscous damping coefficient $k_{M,v}$ | $1.0 \times 10^{-2}$ kg $s^{-1}$ |
| Equilibrium distance $r_{M,0}$ | $6.28 \times 10^{-3}$ m |

**Table 5**
Fluid parameters.

| SPH Parameter Fluid | Value mini-USP II | Value Colon |
|---|---|---|
| Number of SPH particles (fluid) | 131,442 | 64,298 |
| Mass of each particle $m_{Fluid}$ | $8.06 \times 10^{-7}$ kg | $4.72 \times 10^{-6}$ kg |
| Density (fluid) $\rho_{Fluid}$ | 1000 kg m$^{-3}$ | 1000 kg m$^{-3}$ |
| Dynamic viscosity (fluid) $\eta_{Fluid}$ | 1 mPa s | 1 mPa s |

particles $i$ and $j$. $r_0$ is the equilibrium distance between these particles. The Hookean coefficient used for the lattice of the membrane is $k_{M,b}$ and for the springs that return the particles to their initial position is $k_{M,p}$.

To improve the stability of the simulation and to give viscoelastic properties to the membrane (e.g., as in (Sahputra et al., 2020)), an additional viscous force of the following form is added to the membrane particles:

$$F_i = -k_{M,v} v_i \tag{4}$$

Here, $v_i$ is the particle velocity, and $k_{M,v}$ is a viscous damping coefficient.

After calculating all the forces acting on each particle, the particles move according to Newton's equation of motion

$$m_i \frac{d\mathbf{r}_i}{dt} = \sum_j^N F_{ij}, \tag{5}$$

where $\mathbf{r}_i$ is the position of particle $i$.

Further details of the simulated membrane are shown in Table 4.

**Table 6**
Fundamental model parameters.

| Parameter | Value mini-USP II | Value Colon |
|---|---|---|
| **SPH** | | |
| Artificial speed of sound $c_0$ | 0.5 m s$^{-1}$ | 0.1 m s$^{-1}$ |
| Time-step $\Delta t$ | $1.0 \times 10^{-5}$ s | $5.0 \times 10^{-4}$ s |
| Momentum – Smoothing length (fluid) $h_{M,F}$ | $2.45 \times 10^{-3}$ m | $2.45 \times 10^{-3}$ m |
| Momentum – Smoothing length (tablet) $h_{M,T}$ | $1.76 \times 10^{-3}$ m | $1.76 \times 10^{-3}$ m |
| Momentum – Smoothing length (fluid/tablet) $h_{M,F/T}$ | $1.80 \times 10^{-3}$ m | $1.80 \times 10^{-3}$ m |
| Diffusion – Smoothing length (fluid/tablet) $h_{D,F/T}$ | $1.39 \times 10^{-3}$ m | $1.39 \times 10^{-3}$ m |
| Diffusion – Smoothing length (fluid) $h_{D,F}$ | $2.45 \times 10^{-3}$ m | $2.45 \times 10^{-3}$ m |
| Diffusion – Smoothing length (tablet) $h_{D,T}$ | $1.14 \times 10^{-3}$ m | $1.14 \times 10^{-3}$ m |
| Diffusion coefficient (tablet) $D_T$ | $1.0 \times 10^{-30}$ m$^2$s$^{-1}$ | $1.0 \times 10^{-30}$ m$^2$ s$^{-1}$ |
| Diffusion coefficient (fluid/tablet) $D_{F/T}$ *(varies between simulation)* | $8.0 \times 10^{-6}$ m$^2$ s$^{-1}$ $8.0 \times 10^{-7}$ m$^2$ s$^{-1}$ $8.0 \times 10^{-8}$ m$^2$ s$^{-1}$ $8.0 \times 10^{-9}$ m$^2$ s$^{-1}$ $8.0 \times 10^{-10}$ m$^2$ s$^{-1}$ | $8.0 \times 10^{-8}$ m$^2$ s$^{-1}$ |

## 2.4. Fluid

The fluid volume in the mini-USP II is modelled with 131,422 SPH particles corresponding to a fluid volume of 100 mL as used in Stamatopoulos et al. (2015). The number of fluid particles used in the mini-USP II results from several simulations performed with different resolutions. By comparing the velocity fields obtained, the simulation with approximately 130,000 fluid particles proved to be the best compromise between accuracy and computational time.

The resolution obtained in the mini-USP II was accordingly also used in the colon models. Both models account for the same filling level of luminal content, modelled with approximal 64,000 SPH particles. The fluid level is taken from the study of Badley et al. (1993), where they measure the fluid volume in the ascending colon using scintigraphy. The colonic fluid volume found in this study corresponds to a filling level of about 40% in the ascending colon (Prasanth et al., 2012), which is accordingly used in the simulations.

In all models, the fluid is modelled as a Newtonian fluid; more complex rheology could be incorporated with the method developed in Duque-Daza and Alexiadis (2021).

Further details of the fluid used in the mini-USP II and colon model is given in Table 5.

### 2.4.1. Fluid structure interactions

In SPH, the equations of motion result from the discrete approximations of the Navier-Stokes equation on a number of points, which result from the discretisation of the continuum domain. These points can be considered as particles characterised by their mass, velocity, pressure, and density. SPH is based on the mathematical identity:

$$f(\mathbf{r}) = \iiint f(\mathbf{r}') \delta(\mathbf{r} - \mathbf{r}') d\mathbf{r}', \tag{6}$$

where $f(\mathbf{r})$ is any scalar function defined over the volume $V$, with vector $\mathbf{r}$, a position vector in the space $V$. In the SPH formulations, the three-dimensional delta function $\delta(\mathbf{r})$ is approximated by a smoothing kernel $W$ with its characteristic smoothing width or smoothing length $h$:

$$\lim_{h \to 0} W(\mathbf{r}, h) = \delta(\mathbf{r}) \tag{7}$$

Several kernel functions can be found in the literature. In this study, we use the simple Lucy kernel (Lucy, 1977). By replacing the delta function in Eq. (6) with a kernel or smoothing function W, the equation becomes

$$f(\mathbf{r}) \approx \iiint f(\mathbf{r}') W(\mathbf{r} - \mathbf{r}', h) d\mathbf{r}'. \tag{8}$$

By discretising the identity equation over a series of particles of mass $m = \rho(\mathbf{r}') d\mathbf{r}'$, the equation results in

$$f(\mathbf{r}) \approx \sum_i \frac{m_i}{\rho_i} f(\mathbf{r}_i) W(\mathbf{r} - \mathbf{r}_i, h), \tag{9}$$

where $m_i$ is the mass and $\rho_i$ is the density of the $i$th particle. $i$ ranges over all particles within the smoothing kernel $W$ (i.e., $|\mathbf{r} - \mathbf{r}_i| < h$). The Navier-Stokes equation can be approximated by Eq. (9) which represents a discrete approximation of a generic continuous field:

$$m_i \frac{dv_i}{dt} = \sum_j m_i m_j \left( \frac{P_i}{\rho_i^2} + \frac{P_j}{\rho_j^2} + \prod_{i,j} \right) \nabla_j W_{i,j} + \mathbf{f}_i . \tag{10}$$

Here, $v_i$ represents the velocity of particle $i$, $P$ is the pressure, and $W_{i,j}$ is the concise form of $W(|\mathbf{r}_j - \mathbf{r}_i|, h)$. The term $\nabla_j$ is the gradient of the kernel with respect to the coordinate $\mathbf{r}_j$, and $\mathbf{f}_i$ denotes a body force (e.g., gravity). $\Pi_{i,j}$ represents the viscous forces. In literature, various expressions are available for the tensor $\Pi_{i,j}$. Here we use the expression from (Morris et al., 1997)

**Table 7**

Tablet parameters.

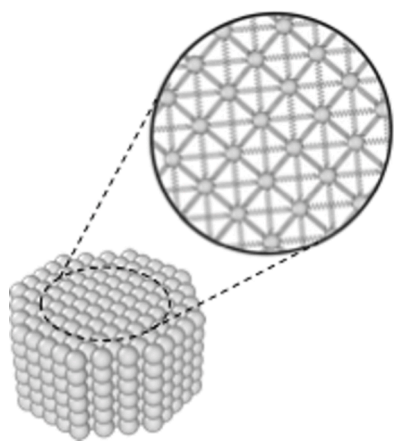| Parameter Tablet | Value |
|---|---|
| **SPH** | |
| Number of SPH tablet particles | 582 |
| Mass of each particle $m_{Tablet}$ | $9.73 \times 10^{-7}$ kg |
| Density (Tablet) $\rho_{Tablet}$ | 1502 kg $m^{-3}$ |
| **LSM** | |
| Hookean coefficient $k_{T,b}$ | 0.1 J $m^{-2}$ |
| Equilibrium distance (linear bonds) $r_{TL,0}$ | $8.8 \times 10^{-4}$ m |
| Equilibrium distance (diagonal bonds) $r_{TD,0}$ | $1.24 \times 10^{-3}$ m |



**Fig. 3.** 3D-representation of the tablet. Linear and diagonal springs connect the particles representing the tablet to obtain a solid structure.

$$\Pi_{i,j} = \frac{(\mu_i + \mu_j)v_{i,j}}{\rho_i\rho_j\mathbf{r}_{i,j}}, \tag{11}$$

where μ is the dynamic viscosity, and $\rho$ is the density of particles $i$ and $j$, respectively. $v_{i,j}$ is the relative velocity.

The Tait equation is used to calculate the pressure forces between the fluid particles and to link the density $\rho$ and the pressure $P$ in Eq. (10):

$$P = \frac{c_0^2\,\rho_0}{7}\left[\left(\frac{\rho}{\rho_0}\right)^7 - 1\right], \tag{12}$$

where $c_0$ is the reference speed of sound and $\rho_0$ is the density at zero applied stress.

For the solid-fluid interactions (i.e., between the container and the fluid, the agitator and the fluid, the membrane and the fluid, and the tablet and the fluid), a repulsive potential in the form

$$E_{ij} = A\left[1 + cos\left(\frac{\pi\,r_{ij}}{r_c}\right)\right] \; with \; r_{ij} < r_c \tag{13}$$

is used. Here, $A$ is an energy constant, $r_{ij}$ represents the distance between particles $i$ and $j$. $r_c$ is the cut-off distance. Viscous forces approximate the no-slip boundary conditions between the solid and fluid particles. These forces are similar to those of Eq. (11) but are applied to the interaction between solid and fluid particles.

Further details of the fundamental simulation parameters are given in Table 6.

### 2.5. Tablet

In our model, the tablet is modelled similarly to Schütt et al. (2021). The tablet is composed of 582 LSM particles and has a total weight of 566 mg, which corresponds to the tablet in Stamatopoulos et al. (2015). The adjacent particles of the tablet are interconnected with linear and diagonal springs to archive a rigid structure according to Eq. (3). The Hookean coefficient used for the lattice of the tablet is $k_{T,b}$ and can be found in Table 7. The tablet is modelled accordingly to the tablet used in Stamatopoulos et al. (2015): a cylindrical body with a height of $5.0 \times 10^{-3}$ m and a diameter of $1.0 \times 10^{-2}$ m. A schematic 3D representation is shown in Fig. 3. The magnification in the figure shows the linear and diagonal bonds of the neighbouring tablet particles.

#### 2.5.1. Tablet disintegration

The dissolution/disintegration process of the tablet is modelled similarly to Schütt et al. (2021). Each of the 582 LSM particles representing the tablet is assigned a specific concentration representing the tablet's active pharmaceutical ingredient (API). The dissolution of the tablet is achieved by mass diffusion between the fluid and tablet particles and between the tablet particles themselves. In the SPH framework, the diffusive mass balance for a multi-component system can be written in the following form (Alexiadis, 2015):

$$\frac{dw_i}{dt} = -\sum_j \frac{m_i m_j}{\rho_i\rho_j} \frac{(D_i + D_j)(C_i - C_j)}{r_{i,j}^2} r_{i,j}\cdot\nabla_j W_{i,j}. \tag{14}$$

Here, $w_i$ is the mass of the fluid in the particle, and $D_i$ is the diffusion coefficient. $C_i$ is the concentration that belongs to each particle $i$. Eq. (15) is used to close Eq. (14) with the following relation between $m_i$, $C_i$ and $\rho_i$ (Alexiadis, 2015):

$$w_i = C_i\frac{m_i}{\rho_i} \tag{15}$$

The API used in the experimental tablet from Stamatopoulos et al. (2015) is Theophylline (THE), a highly water-soluble drug. The solubility of THE in water at 37 °C is approximately 12.5 mg mL$^{-1}$ (Grassi et al., 2001). This means it is possible to dissolve the entire tablet in the fluid volume within these models. The diffusion coefficient of THE was determined in distilled water and estimated to be $8.21 \times 10^{-10}$ m$^2$ s$^{-1}$ (Grassi et al., 2001).

The tablet is modelled as 100% drug and we assume that the drug is uniformly distributed within the real tablet. We are aware that the tablet used in Stamatopoulos et al. (2015) contains excipients (e.g., to control the drug release) and not only drug. However, this study focuses on the tablet's realistic dissolution/disintegration behaviour and not on the influence of different excipient compositions on the dissolution/disintegration behaviour. We indirectly accounted for the influence of excipients on tablet dissolution/disintegration by using experimental tablet optimisation data and modifying the modelled tablet to behave like the experimental tablet as a whole (i.e., drug + excipients).

In the tablet model, all the neighbouring particles are interconnected with each other with bonds. If the concentration of at least one of two adjacent tablet particles falls below a predefined threshold $X$ (e.g., $X = 0.90$ means 10% dissolved), the bond between these particles is removed weakening the solid structure of the tablet. A bond between two particles is also deleted if the distance between two bonded particles increases by 10% of their initial spacing (e.g., due to the influence of shear forces). If a computational tablet particle has no bond with any other tablet particles, the particle detaches completely from the tablet. In this way, the disintegration process of the tablet is simulated.

Finally, when the concentration of the active ingredient in the tablet is below its solubility concentration $C_S$ (defined as 5%, i.e., 95% dissolved), the type of the tablet particle is changed from LSM to SPH: i.e., the particle stops behaving like a solid particle and behaves like a fluid particle.

In the models (i.e., mini-USP II and colon), the fluid and the tablet were discretised differently (i.e., different particle resolution). This results in a different initial particle distance between the fluid and the tablet particles. Thus, a different 'momentum' smoothing length is used between the fluid and tablet particles. The 'diffusion' smoothing length
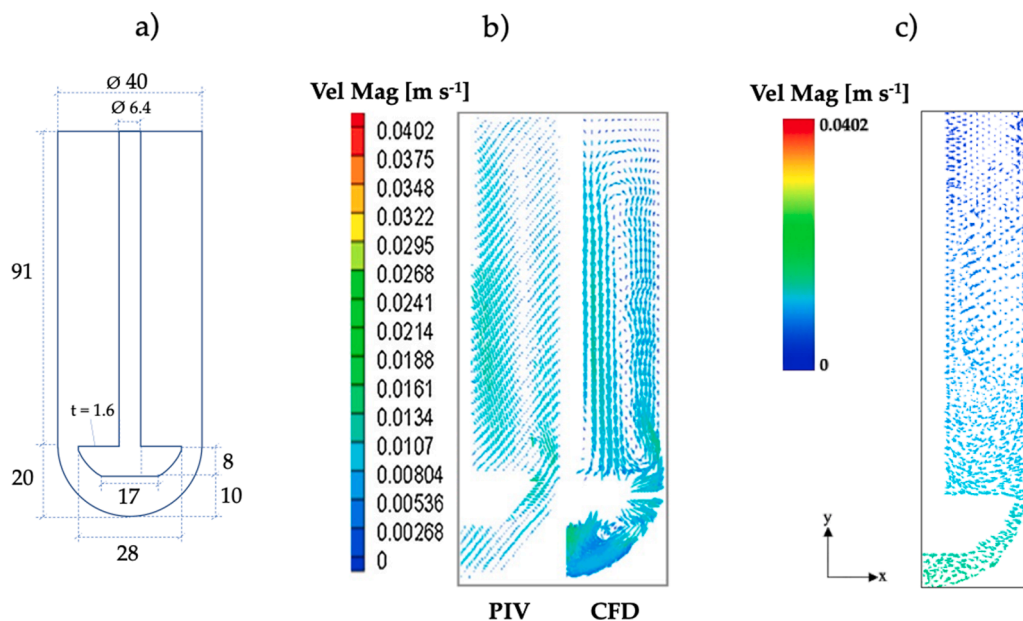
**Fig. 4.** Validation of the computational mini-USP II model by comparison of the velocity profile from the simulation with experimental and simulated data from Wang and Armenante (2016). (a) shows the dimensions of the mini-USP II used in both, the experimental and computational part, (b) Experimental and computational data reproduced with permission from Wang et al., and (c) the velocity profile obtained from the simulation.

between the fluid and tablet particles is obtained from a weighted smoothing length based on the smoothing length of the fluid particles and the tablet particles. Further details of the general model parameter and specific model properties are given in Table 6 and Table 7, respectively.

### 2.5.2. Development of the tablet and data analysis

The simulation of a disintegrating/dissolving tablet in a stirring tank with SPH is computational very intensive. In our case, to simulate approximately 2 min of real-time 144 cores with 576 GB memory, a wall time of 10 days is needed.

To overcome this problem, we notice that the time scale of the hydrodynamics $T_H$ in the stirring tank and the time scale of the tablet dissolution process $T_D$ are different (i.e., $T_H \sim 1$ s and $T_D \sim 1$ hour) and do not overlap ($T_D >> T_H$). Since the tablet dissolution is considerably slower than the hydrodynamics, we can assume that, if we consider small time intervals of the order of $T_H$, the dissolution process does not affect the hydrodynamics. Furthermore, the results of the dimensional analysis (Section 2.2.2) confirms that it is possible to compare different diffusion coefficients $D$ by rescaling time $t$, because $t$ is inversely proportionally to the diffusion coefficient:

$$t \propto \frac{1}{D}, \tag{16}$$

By using Eq. (16), it is possible to compare the dissolution profiles of tablets with different diffusivities. For instance, the dissolution profile of a tablet with total dissolution time $t_0 = 10^4$ s and $D = 10^{-10}$ m$^2$ s$^{-1}$ has the same shape of the dissolution profile of a tablet with $t_0 = 1$ s and $D = 10^{-6}$ m$^2$ s$^{-1}$. That is, if we use dimensionless numbers, these two profiles overlap. In the next sections, we are going to use a dimensional time $\tau$ defined as

$$\tau[-] = \frac{t}{t_0}, \tag{17}$$

where $t_0$ is the total dissolution time and $t$ is the actual time. For the simulation data $t_0 = 90$ s and for the experimental data of Stamatopoulos et al. (2015) $t_0 = 18000$s.

Stamatopoulos et al. (2015) analysed the dissolution process in the mini-USP II across a time interval of approximately 8 hours,

corresponding to a time scale of $10^4$ s. The diffusion coefficient of the pure drug used in the experimental tablet is approximately $8.0 \times 10^{-10}$ m$^2$ s$^{-1}$.

In order to find a tablet that behaves as similarly as possible to the experimental one, we built tablets with different thresholds $X$: 0.1, 0.35, 0.60, and 0.85 (see Section 2.5.1). This means that the bond between two tablet particles breaks when 90%, 65%, 40%, or 15%, respectively, of the API concentration of the bound particles, is dissolved in the fluid. Simulations were carried out with the modelled tablets and with different diffusion coefficients of the API: $8.0 \times 10^{-6}$ m$^2$ s$^{-1}$, $8.0 \times 10^{-7}$ m$^2$ s$^{-1}$, $8.0 \times 10^{-8}$ m$^2$ s$^{-1}$, $8.0 \times 10^{-9}$ m$^2$ s$^{-1}$, and $8.0 \times 10^{-10}$ m$^2$ s$^{-1}$.

Data analysis of the different tablets and diffusion coefficients $D$ shows (Section 3.2) that the API mass flow $\phi$ * for each tablet follows the following equation:

$$\phi^* = \epsilon D^\alpha, \tag{18}$$

where $\epsilon$ is a tablet specific constant and $\alpha = 0.61$ an exponential constant valid for all tablets.

To determine the model that best represents the behaviour of the experimental tablet from Stamatopoulos et al. (Stamatopoulos et al., 2015), the Péclet number *Pe* was used:

$$Pe = \frac{N\, d^2}{D}, \tag{19}$$

where $N$ is the paddle speed, $d$ the paddle diameter and $D$ the diffusion coefficient.

The experimental dissolution data from Stamatopoulos et al. (2015) show a linear progression (see Section 3.2 Fig. 10) and an average mass flow rate of the API from the tablet of approximately $8.29 \times 10^{-9}$ kg s$^{-1}$. The corresponding *Pe* number for these conditions is $9.15 \times 10^5$. Due to the limited data available, only this single data point is used to select the computational tablet whose dissolution profile best matches the behaviour of the real tablet.

### 2.6. Software

The simulations in this study were performed using the University of Birmingham's BlueBEAR HPC service (Birmingham, 2021). For the
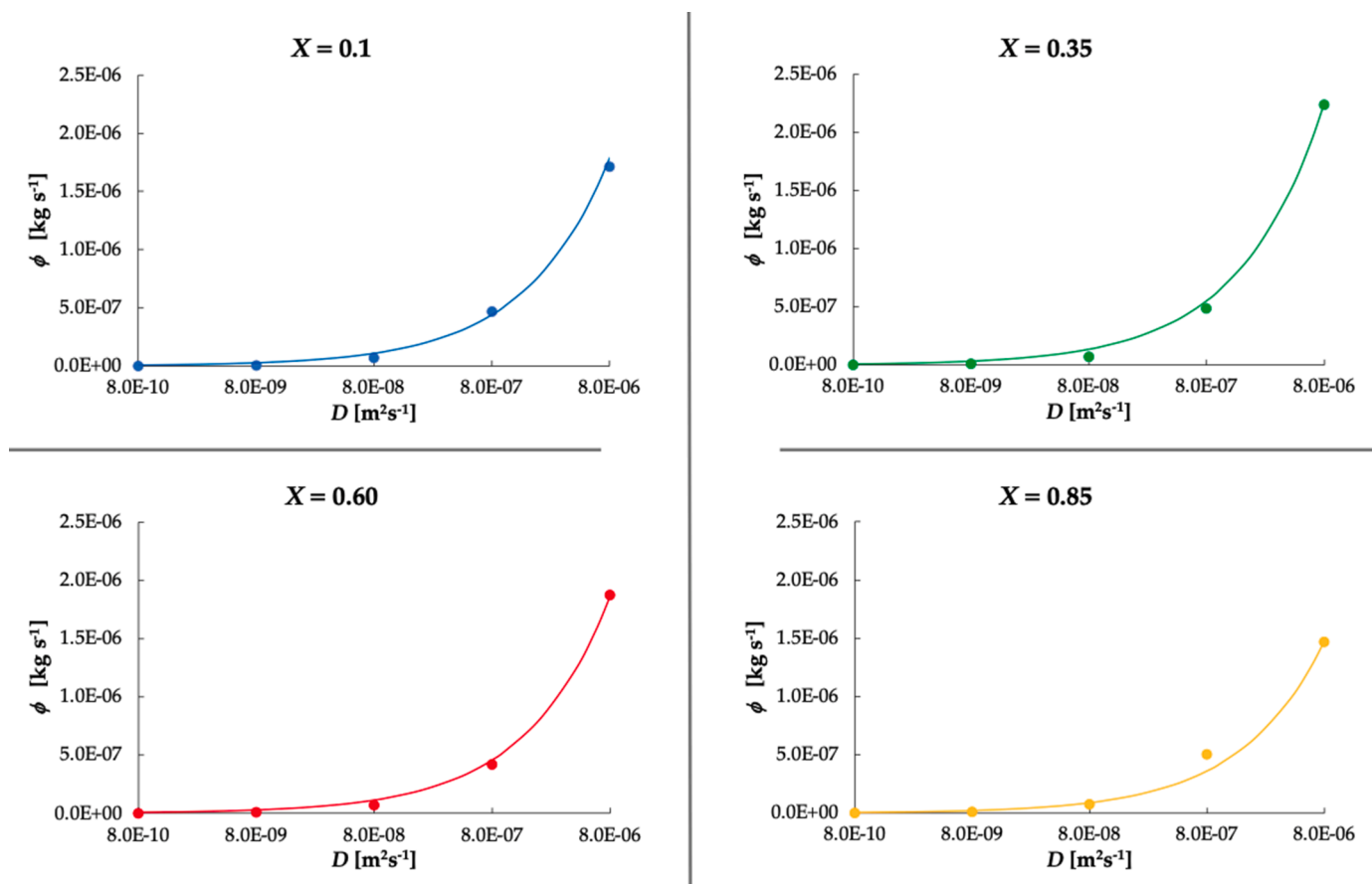
**Fig. 5.** Mass flow rate φ of the API from the tablet obtained from the simulations in the mini-USP II for different X and for different diffusion coefficients D.

numerical calculations, the open-source code LAMMPS (Ganzenmüller et al., 2011; Plimpton, 1995) is used. OVITO (Stukowski, 2010) is used for the visualisation and MATLAB (MATLAB 2022) for the post-processing of the simulation data.

## 3. Results and discussion

### 3.1. Model validation - hydrodynamics

To validate our computational model of the mini-USP II in terms of hydrodynamics, we compared the obtained velocity profile with experimental and computational data from Wang et al. (Wang and Armenante, 2016). The experimental data were determined using Particle Image Velocimetry (PIV). The computational data were obtained by using ANSYS GAMBIT 2.4.6.

Fig. 4a) represents the dimensions of the mini-USP II used by Wang et al. (Wang and Armenante, 2016), Fig. 4b) the experimental and computational results obtained from Wang et al. and Fig. 4c) the result from the DMP simulation. The DMP model shows good agreement with the results of Wang et al. (Wang and Armenante, 2016).

### 3.2. Evaluation of the tablet disintegration/dissolution

As discussed in Section 2.5.2, four different tablets with different threshold values X (i.e., value for the bond/break specification) and different diffusion coefficients have been developed. In total, 20 different simulations were performed to investigate the tablet that best matches the performance of the experimental tablet from Stamatopoulos et al. (2015).

The results from the simulations for each X are represented in Fig. 5.

The data for the different threshold values X show that the Mass flow

**Table 8**
Values for the constant ε..

| X | ε |
|---|---|
| 0.1 | $2.3 \times 10^{-3}$ |
| 0.35 | $2.9 \times 10^{-3}$ |
| 0.60 | $2.4 \times 10^{-3}$ |
| 0.85 | $1.9 \times 10^{-3}$ |

rate of the API from the tablet can be represented by Eq. (18). The exponential constant was determined to be α = 0.61. The values for ε are shown in Table 8:

Fig. 6(a) shows the entire diagram of the simulations, where the mass flow rate φ * (i.e., calculated using Eq. (18)) of the different computational tablets is represented over the Péclet number. The red star indicates the data point of the experimental tablet.

To be able to analyse the region of the experimental tablet (i.e., with the red star) more precisely, an enlarged section of this region is shown in Fig. 6b).

From Fig. 6b) it can be observed that the modelled tablet with a bond/break threshold X = 0.35 best represents the behaviour of the experimental tablet.

To further verify the realistic disintegration behaviour of the modelled tablet, the disintegration course of the modelled tablet was compared with the disintegration course of a real tablet. Unfortunately, the tablet used in Stamatopoulos et al. (Stamatopoulos et al., 2015) is customized and therefore not available for direct comparison. Nevertheless, to be able to compare the disintegration process of the modelled tablet with a real tablet, we used a commercially available tablet. The reference tablet shown in Fig. 7 (top) is an immediate-release (IR) tablet (i.e., Metoprolol tartrate, an oral administered tablet) from Aurobindo
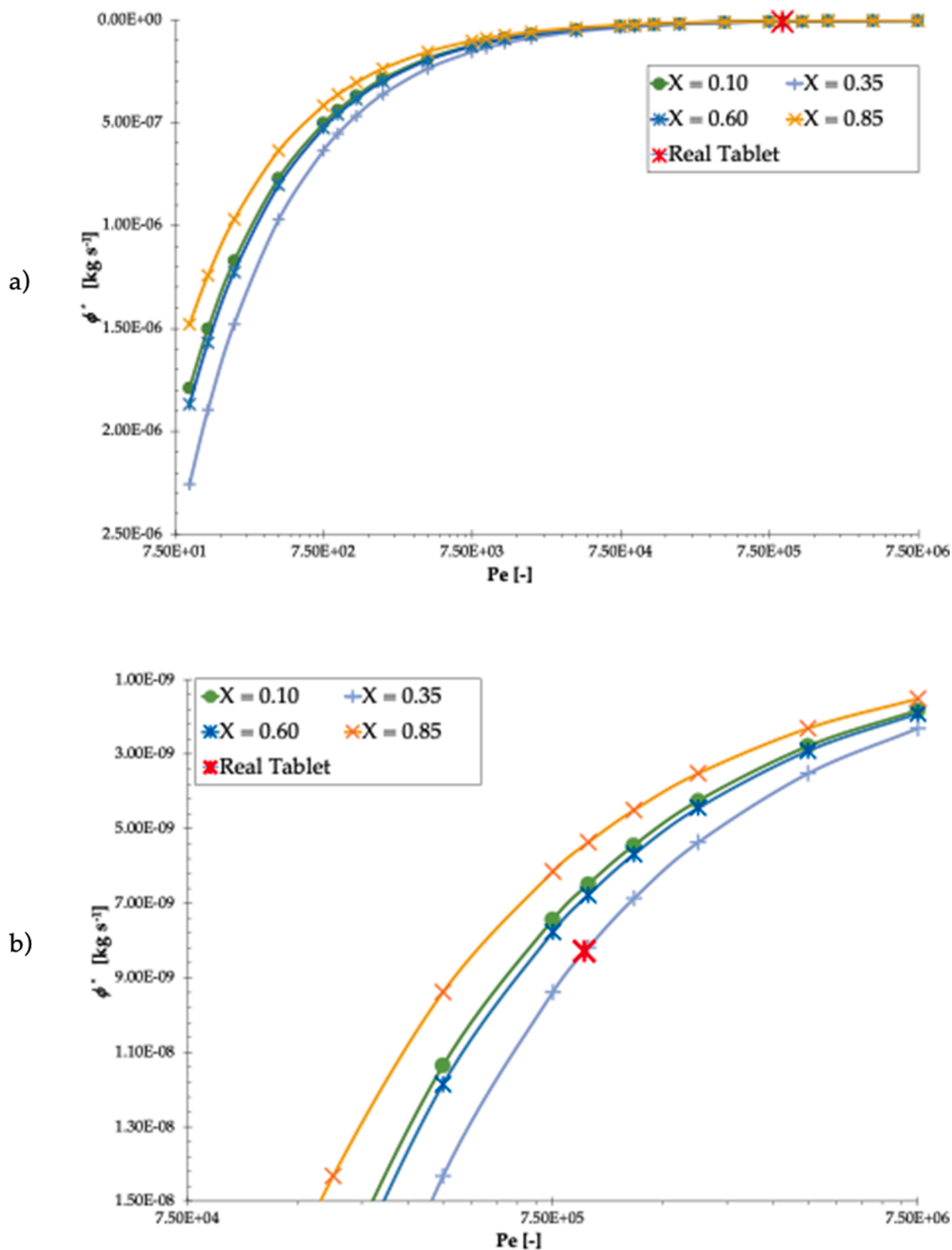
**Fig. 6.** a) Representation of the results obtained from the simulations and a characteristic data point from the experimental tablet. b) Enlarged section from a) of the region of the experimental tablet.

Pharm - Milpharm Ltd. Images of the disintegration/dissolution process of the tablet were taken at four different time points, each fifteen minutes apart. The conditions in the mini-USP II were similar to the model conditions: rotational speed of the paddle 50 rpm, water temperature 37 °C.

In Fig. 7, the tablet is in its initial rigid state at $t_0$ and slowly disintegrates from the left to the right. The computational tablet shows a very similar behaviour to the real tablet. At Phase = 0, water diffuses into the tablet and some tablet particles detach from the tablet. From Phase = 1 to Phase = 4, the tablet shape changes in both cases, the computational and the real tablet, from a cylindrical body to a cone and releases more and more particles. The fact that the disintegrating tablet
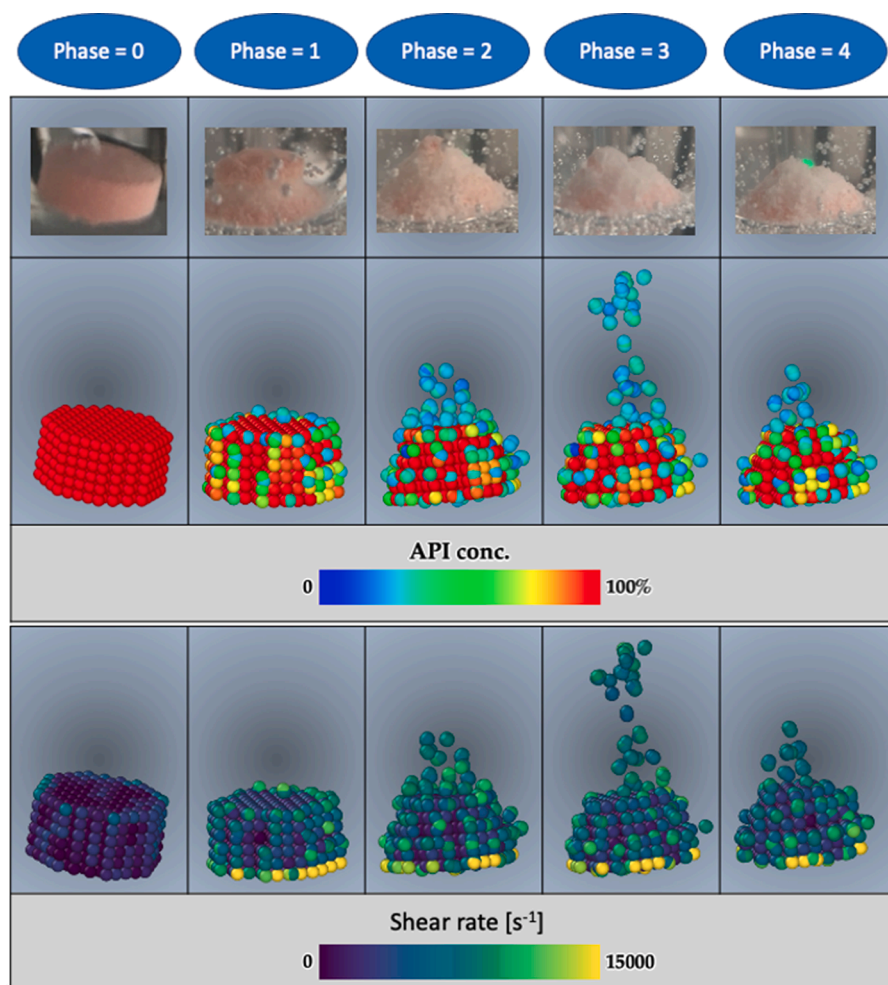
**Fig. 7.** Comparison of the tablet disintegration/dissolution process of a real tablet (top) and the computational tablet (middle and bottom) at different phases of the tablet disintegration/dissolution process. The particles of the modelled tablet (middle) are coloured according to their API concentration, where red indicates 100% API and dark blue 0% API. At the bottom the particles of the modelled tablet are coloured according to the shear rate exposed, where purple indicates low, and yellow a high shear rate.

forms a cone is a typical picture in the USP II dissolution apparatus and a result of the lower hydrodynamics below the paddle (Pepin et al., 2022).

The drug release process from the tablet and the disintegration/dissolution of the tablet occurs in four main steps as shown in Fig. 8. As an example, we used the tablet that represents the real tablet and scaled the time and the diffusion coefficient according to Eq. (16). Thus, we use a diffusion coefficient of $D = 8.0 \times 10^{-6}$ m$^2$ s$^{-1}$ for the simulation and run the simulation for 120 s real time.

In the first step, water diffuses into the tablet and the API into the fluid, resulting in an almost linear release of active ingredient. In the second step, the rigid structure of the tablet begins to weaken, and the first drug particles detach from the tablet into the fluid. In our case, a particle that detaches from the tablet but is not yet completely dissolved in the fluid is counted as a "tablet particle". The drug release profile is still linear, but with a lower slope. The outer layer absorbed water and thus its API content, creating an additional mass transfer resistance between the core of the tablet (rich in drug) and water. In the third step, more particles detach from the tablet. This temporarily leads to an increased release of the API, as a larger part of the tablet is exposed to the fluid. Finally, in the fourth step, the solid structure continues to weaken, resulting in fragments detaching from the tablet, and leading to an increased release of active ingredient.

One main parameter influencing the disintegration/dissolution of the tablet is the shear stress acting on the surface of the tablet (Schütt et al., 2021). Fig. 9 represents the dissolution profile and the average shear rate acting on the tablet particles over time. The profile is taken from the same tablet used in Fig. 8.

In the model, the paddle was 'switched on' and the tablet was 'activated' as soon as the hydrodynamics in the container were steady state. For this reason, the shear rate acting on the tablet is already at a higher value at $t = 0$. In the course of disintegration, the average shear rate also increases. This is because the structure of the rigid tablet becomes weaker and individual particles detach from the tablet, creating edges on the tablet on which the fluid can act more effectively.

The shear stresses and, consequently, shear rates acting on the tablet surface are in good in agreement with the shear stresses found in Kindgen et al. (Kindgen et al., 2015), where they performed simulations of the hydrodynamics and stresses in the PhEur/USP Disintegration Tester with different fluids (i.e., Newtonian and non-Newtonian fluids and different fluid viscosities). These values also correspond very well with the shear stresses found in other studies, even though they focused on the stomach (Abrahamsson et al., 2005; Pal et al., 2003).

In Fig. 10, the drug release data from the modelled tablet obtained in the mini-USP II model is compared to the experimental data from Stamatopoulos et al. (2015). This is done using the dimensionless time $\tau$ (Eq. (17)). Stamatopoulos et al. (2015) received the drug release data using two different sampling points $S_p$ in the mini-USP II container (i.e., 19 and 66 mm above the paddle). For comparison, we use an average of these measurements, indicated as Stamatopoulos et al. 'average' in Fig. 10.

The standard deviation $s$ in Fig. 10 is calculated as follows:

$$s = \frac{\left| S_{p,2} - S_{p,2} \right|}{\sqrt{2}}, \tag{20}$$

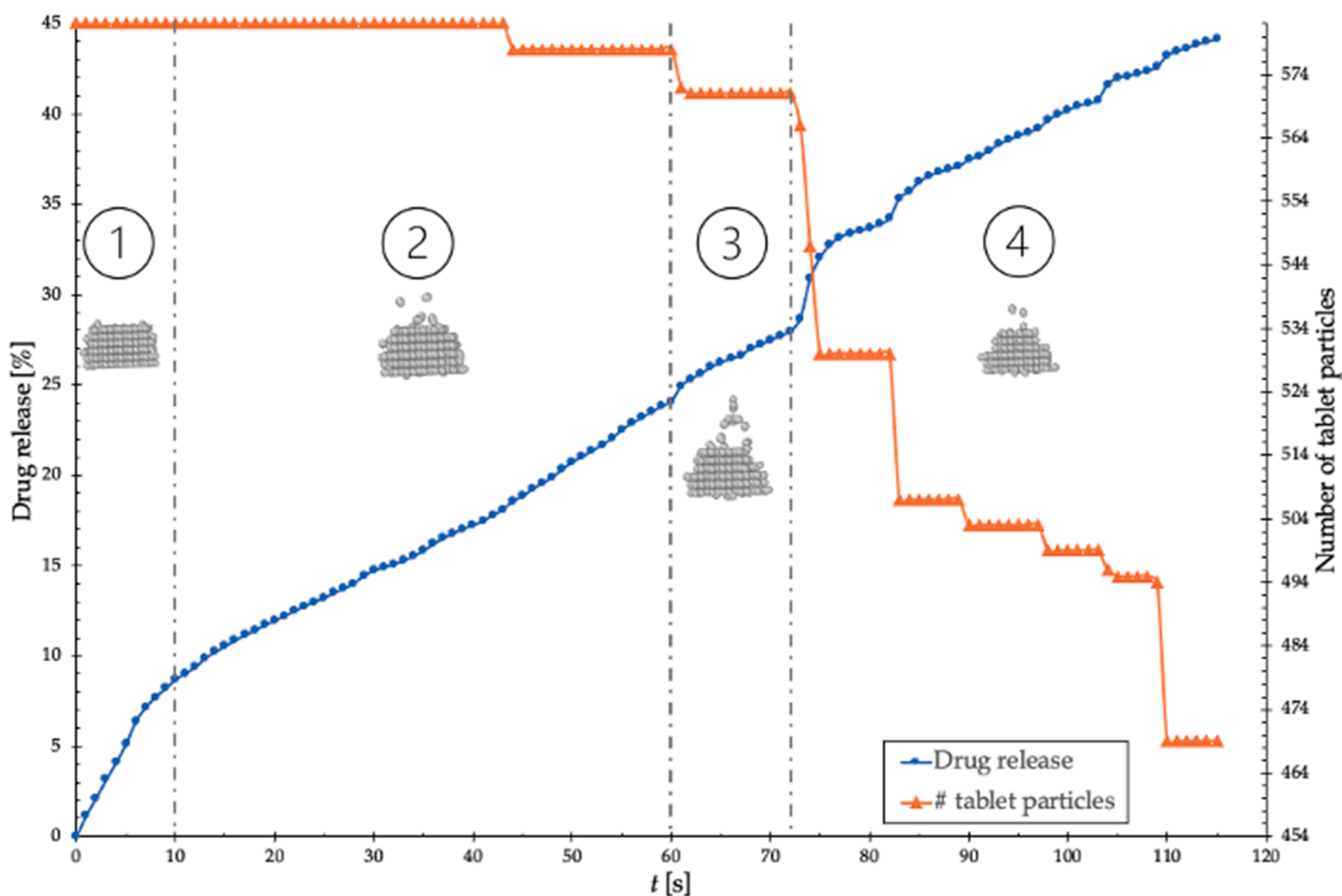**Fig. 8.** Drug release and tablet disintegration of the modelled tablet in the mini-USP II with X = 0.35 and D = $8.0 \times 10^{-6}$ m$^2$ s$^{-1}$. The blue line represents the drug release and the orange line the number of tablet particles not yet dissolved in the fluid.
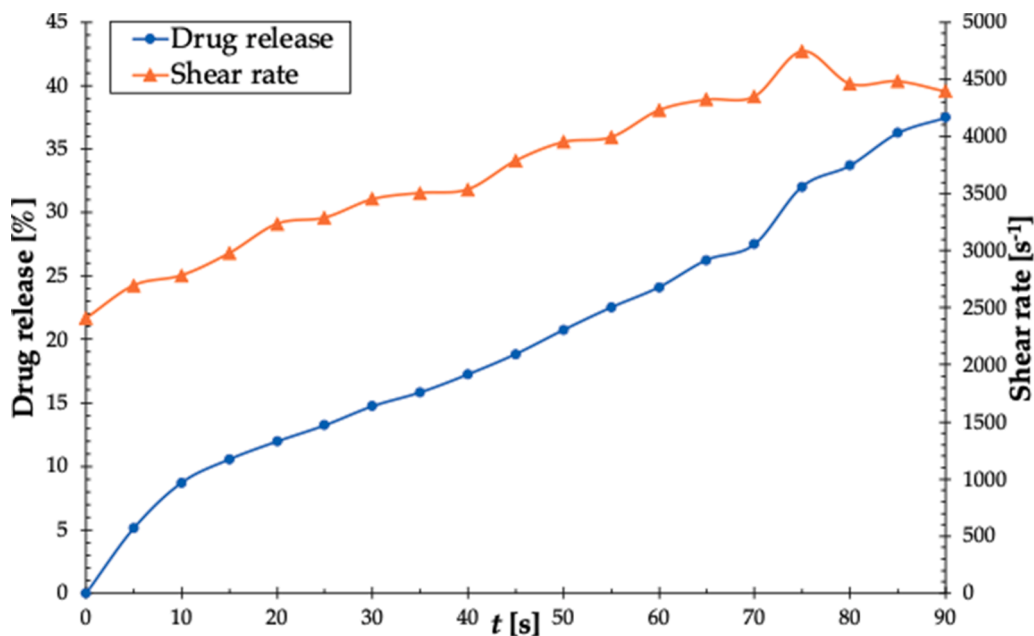


**Fig. 9.** Drug release and tablet disintegration of the modelled tablet in the mini-USP II with X = 0.35 and D = $8.0 \times 10^{-6}$ m$^2$ s$^{-1}$. The blue line represents the drug release and the orange line the average shear stress acting on the tablet particles.

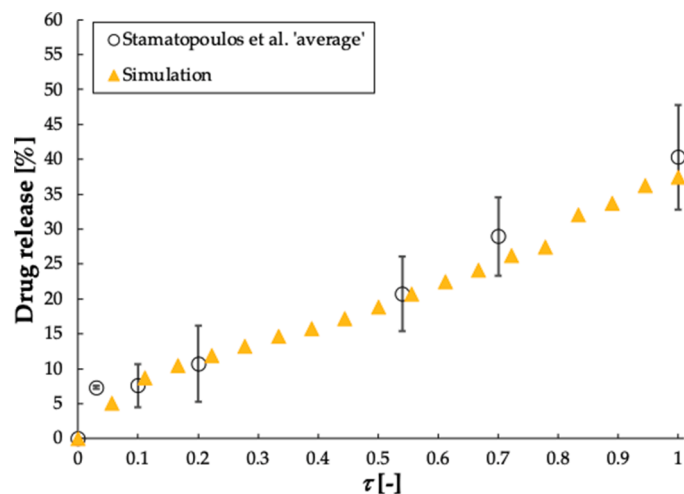**Fig. 10.** Drug release and tablet disintegration of the modelled tablet in the mini-USP II with X = 0.35 and D = $8.0 \times 10^{-6}$ m$^2$ s$^{-1}$ and the experimental data for a simple buffer reproduced from Stamatopoulos et al. (2015).



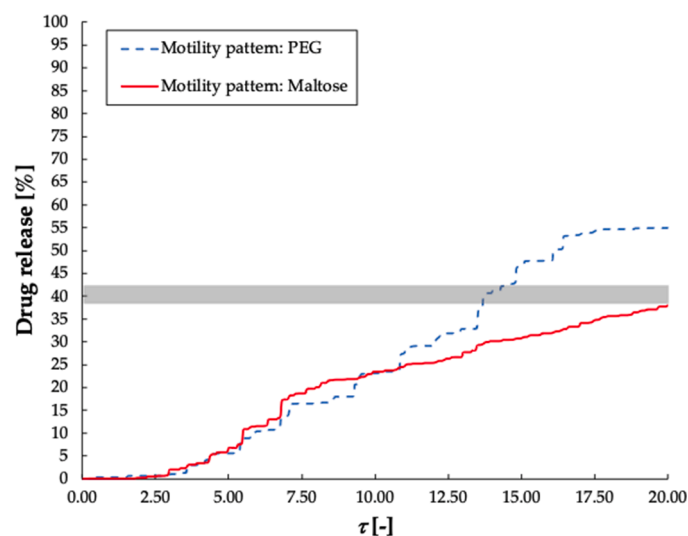**Fig. 11.** Drug release of the modelled tablet with X = 0.35 and D = $8.0 \times 10^{-6}$ m$^2$ $s^{-1}$ in the colon model using two different in vivo motility pattern from Schütt et al. (2021).
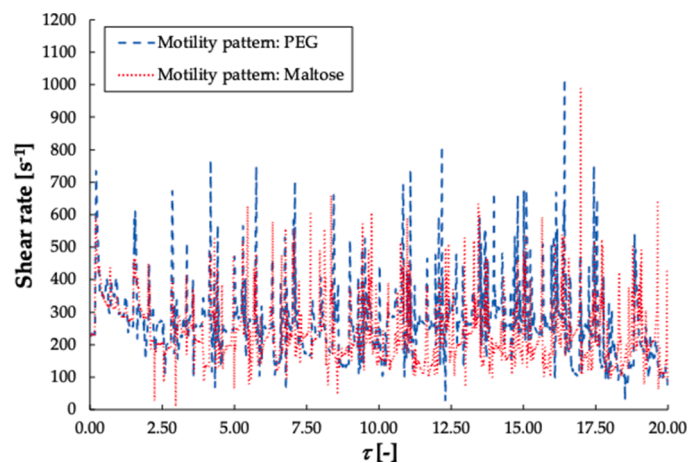


**Fig. 12.** Shear rate acting on the modelled tablet during the drug release process represented in Fig. 11 (colon model).

*3.3. Comparison of the drug release profile from the experimental tablet in the mini-USP II with the drug release profile of the computational tablet in the colon model*

To compare the dissolution profile of the conventional dissolution apparatus with the colon model, we run the simulation with the same tablet properties used in the mini-USP II model (i.e., $D = 8.0 \times 10^{-6}$ m$^2$ s$^{-1}$, $X = 0.35$) in the colon model and determine drug release profile and shear stress acting on the tablet. Fig. 11 shows the drug release profile in the colon models with two different in vivo motility patterns, 'PEG' and 'Maltose' (Schütt et al., 2021). The dimensionless time $\tau$ is calculated according to Eq. (14).

The grey shaded area represents the drug release obtained in the mini-USP II in Fig. 10 at $\tau = 1$. In the colon models, it takes approximately 13.5 times longer in the case of the PEG motility pattern and approximately 20 times longer in the case of the maltose motility pattern to achieve the same drug release as in the mini-USP II.

This can be explained by the shear rate acting on the tablet surface, represented in Fig. 12. In the colon models, the shear stress is induced by the wall motion of the colon.

By comparing Fig. 9 and Fig. 12 (i.e., mini-USP II and colon model, respectively), it can be established that the shear rate acting on the tablet surface in the colon models is about one order of magnitude smaller than in the mini-USP II at 50 rpm. Also, the shear stress profile shows different progress in the mini-USP II compared to the colon model. In the mini-USP II, the shear rate acting on the tablet is rather constant, whereas, in the colon model, it occurs in peaks, which accelerates the drug release process (Schütt et al., 2021).

To investigate whether a slower paddle speed in the mini-USP II results in a shear rate acting on the tablet that is of the same order of magnitude as in the colon model and thus more closely mimics in vivo conditions, we built several mini-USP II models with different paddle speeds. The paddle speed was set to 1, 5, 15, 25, 35 and 50 rpm accordingly. The properties of the tablet are the same as those used previously (i.e., $D = 8.0 \times 10^{-6}$ m$^2$ s$^{-1}$, $X = 0.35$).

Fig. 13 shows the influence of the paddle speed on the tablet's drug release profile in the min-USP II.

With an increased paddle speed and thus a higher fluid flow around the tablet, the drug release process is also accelerated.

Likewise, the shear rate acting in the tablet increases with an increase in paddle speed, which is represented in Fig. 14.

According to Metzner et al. (1961), the average shear rate in the liquid is a function of the impeller speed and behaves proportionally. In this case, the shear rate experienced by the tablet is not proportional to the paddle speed. This can be attributed to the fact that different velocity profiles occur in the container and that the fluid flow around the tablet is not proportionally to the paddle speed. Even at low paddle speeds of 1 and 5 rpm, the average shear stress experienced by the tablet is about one order of magnitude larger than the 'baseline' shear stress acting on the tablet in the colon models (Fig. 12). As mentioned previously, the tablet is 'activated' when the hydrodynamics in the container reaches steady-state conditions. Therefore, the shear stress is already at an increased value at $\tau = 0$. From the results in Fig. 14, even a paddle speed of 1 rpm in the mini-USP II results in a slightly too high average shear rate acting on the tablet compared to the colon models. However, by using an "on-off" operating mode in the mini-USP II, the conditions (i.e., the generation of shear rate peaks) would better reflect the in vivo conditions of the human colon instead of a constant paddle speed of 50 rpm normally used.

## 4. Conclusion

In this study, we reuse a computational model of ascending colon developed in Schütt et al. (2021) with in vivo motility patterns, a digital twin of the mini-USP II dissolution apparatus and a digital twin of a tablet that mimics a real tablet. The models are used to compare the
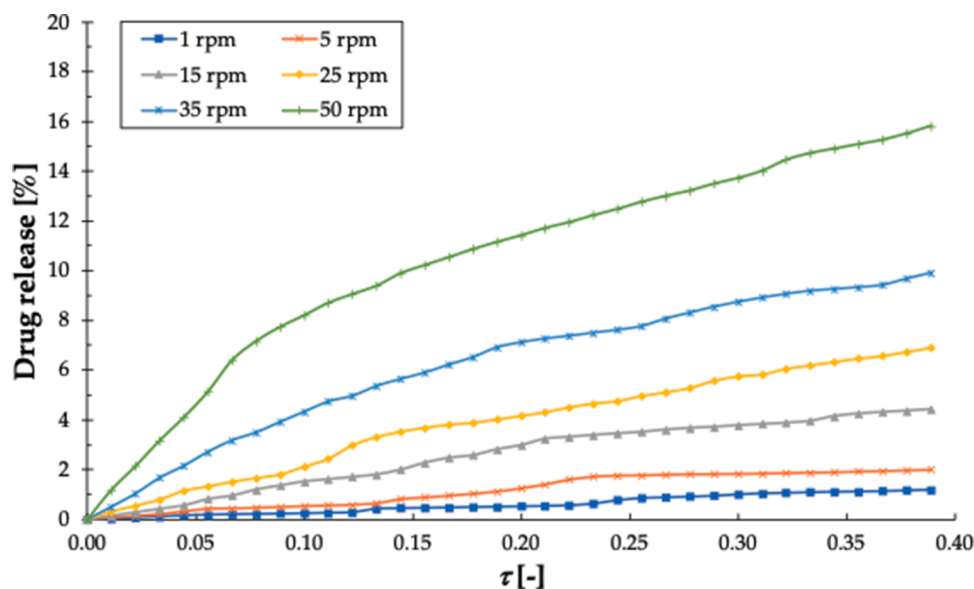
**Fig. 13.** Drug release profile in the mini-USP II at different paddle speeds.
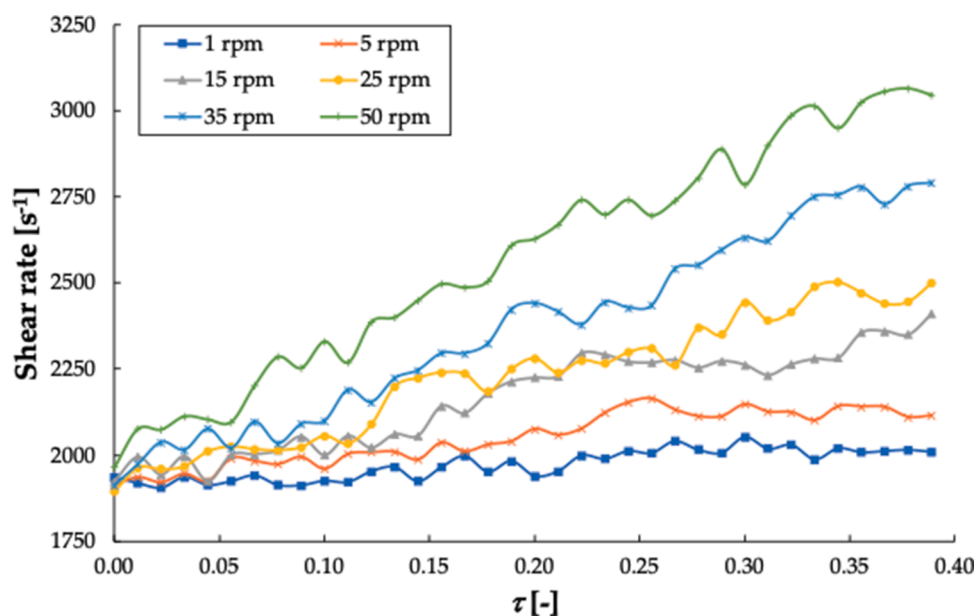


**Fig. 14.** Shear rate acting on the modelled tablet during the drug release process in the mini-USP II shown in Fig. 13.

disintegration/dissolution behaviour of a tablet in a standard dissolution apparatus and a biorelevant colon model. We show the extreme case where the fluid exerts higher shear rates on the tablet surface than a fluid with higher viscosity, as previously demonstrated in Schütt et al. (2021).

The shear rates acting on a tablet surface determined in the colon models are in the same order of magnitude as in Abrahamsson et al. (2005), even though their study focuses on the stomach. This is probably due to elevated colon motility stimulated by PEG and maltose, resulting in increased shear rates that also occur in the fed stomach.

The results show that the average shear forces acting on a tablet are relatively low in the colon models and follow a different pattern than in the mini-USP II. A much lower paddle speed and a structured stirring profile could be used to replicate these conditions better. A different approach could be to lower the "baseline" shear rate acting on the tablet, increased clearance in the mini-USP II could be used. However, whether the mini-USP II or even the USP II dissolution apparatus is the most

appropriate apparatus to mimic in vivo conditions in the colon is worth considering.

The current challenges and limitations of the approach to developing a computational tablet that mimics a real tablet are based on the available experimental data. Future work needs to incorporate more data from the real tablet, such as the release profile at different paddle speeds in the mini-USP II, to support further the accuracy of the method used. Nevertheless, the approach shows a first step towards modelling a real tablet.

**Funding**

## CRediT authorship contribution statement

**M. Schütt:** Conceptualization, Data curation, Methodology, Visualization, Writing – original draft, Writing – review & editing. **K. Stamatopoulos:** Conceptualization, Writing – review & editing. **H.K. Batchelor:** Writing – review & editing. **M.J.H. Simmons:** Writing – review & editing. **A. Alexiadis:** Conceptualization, Data curation, Methodology, Supervision, Writing – review & editing.

## Declaration of Competing Interest

The authors have declared that no competing interests exist.

## Data availability

Data will be made available on request.

## Acknowledgments

## References

Abrahamsson, B., Pal, A., Sjoberg, M., Carlsson, M., Laurell, E., Brasseur, J.G., 2005. A novel in vitro and numerical analysis of shear-induced drug release from extended-release tablets in the fed stomach. Pharm. Res. 22 (8), 1215–1226.

Alexiadis, A., 2014. A smoothed particle hydrodynamics and coarse-grained molecular dynamics hybrid technique for modelling elastic particles and breakable capsules under various flow conditions. Int. J. Numer. Methods Eng. 100 (10), 713–719.

Alexiadis, A., 2015a. The Discrete Multi-Hybrid System for the Simulation of Solid-Liquid Flows. PLoS One 10 (5), e0124678.

Alexiadis, A., 2015b. A new framework for modelling the dynamics and the breakage of capsules, vesicles and cells in fluid flow. Procedia IUTAM 16, 80–88.

Alexiadis, A., 2019. Deep multiphysics: coupling discrete multiphysics with machine learning to attain self-learning in-silico models replicating human physiology. Artif. Intell. Med. 98, 27–34. Jul.

Alexiadis, A., Stamatopoulos, K., Wen, W., Batchelor, H.K., Bakalis, S., Barigou, M., Simmons, M.J.H., 2017. Using discrete multi-physics for detailed exploration of hydrodynamics in an in vitro colon system. Comput. Biol. Med. 81, 188–198.

Ariane, M., Allouche, M.H., Bussone, M., Giacosa, F., Bernard, F., Barigou, M., Alexiadis, A., 2017a. Discrete multi-physics: a mesh-free model of blood flow in flexible biological valve including solid aggregate formation. PLoS One 12 (4), e1002047.

Ariane, M., Kassinos, S., Velaga, S., Alexiadis, A., 2018a. Discrete multi-physics simulations of diffusive and convective mass transfer in boundary layers containing motile cilia in lungs. Comput. Biol. Med. 95, 34–42.

Ariane, M., Vigolo, D., Brill, A., Nash, F.G.B., Barigou, M., Alexiadis, A., 2018b. Using Discrete Multi-Physics for studying the dynamics of emboli in flexible venous valves. Comput. Fluids 166, 57–63. Apr 30.

Ariane, M., Wen, W., Vigolo, D., Brill, A., Nash, F.G.B., Barigou, M., Alexiadis, A., 2017b. Modelling and simulation of flow and agglomeration in deep veins valves using discrete multi physics. Comput. Biol. Med. 89, 96–103.

Badley, A.D., Camilleri, M., Oconnor, M.K., 1993. Noninvasive measurement of human ascending colon volume. Nucl. Med. Commun. 14 (6), 485–489.

Baksamawi, H.A., Ariane, M., Brill, A., Vigolo, D., Alexiadis, A., 2021. Modelling particle agglomeration on through elastic valves under flow. ChemEngineering 5 (3), 40.

Bampton, P.A., Dinning, P.G., Kennedy, M.L., Lubowski, D.Z., deCarle, D., Cook, I.J., 2000. Spatial and temporal organization of pressure patterns throughout the unprepared colon during spontaneous defecation. Am. J. Gastroenterol. 95 (4), 1027–1035. Apr.

U. Birmingham. "University of Birmingham's BlueBEAR HPC service," 01/09/2021, 2021; http://www.birmingham.ac.uk/bear.

Dinning, P.G., Szczesniak, M.M., Cook, I.J., 2008. Proximal colonic propagating pressure waves sequences and their relationship with movements of content in the proximal human colon. Neurogastroenterol. Motil. 20, 512–520.

Duque-Daza, C., Alexiadis, A., 2021. A simplified framework for modelling viscoelastic fluids in discrete multiphysics. Chemengineering 5 (3). Sep.

G.C. Ganzenmüller, M.O. Steinhauser, and P. Van Liedekerke, "The implementation of smoothed particle hydrodynamics in LAMMPS," *Retrieved from (lammps.sandia.gov/doc/PDF/SPH_LAMMPS_userguide.pdf),* vol. (last accessed 17.10.2019), 2011.

Grassi, M., Colombo, I., Lapasin, R., 2001. Experimental determination of the theophylline diffusion coefficient in swollen sodium-alginate membranes. J. Controlled Rel. 76 (1), 93–105, 2001/09/11/.

Hopgood, M., Reynolds, G., Barker, R., 2018. Using computational fluid dynamics to compare shear rate and turbulence in the TIM-automated gastric compartment with USP Apparatus II. J. Pharm. Sci. 107 (7), 1911–1919. Jul.

Kindgen, S., Wachtel, H., Abrahamsson, B., Langguth, P., 2015. Computational fluid dynamics simulation of hydrodynamics and stresses in the pheur/usp disintegration tester under fed and fasted fluid characteristics. J. Pharm. Sci. 104 (9), 2956–2968. Sep.

Klein, S., Shah, V., 2008. A standardized mini paddle apparatus as an alternative to the standard paddle. AAPS PharmSciTech. 9 (4), 1179–1184. Dec.

Kot, M., 2021. Mass spring models of amorphous solids. Chemengineering 5 (1). Mar.

Kot, M., Nagahashi, H., Szymczak, P., 2015. Elastic moduli of simple mass spring models. Visual Computer 31 (10), 1339–1350.

Liu, G.R., Liu, M.B., 2003. Smoothed Particle Hydrodynamics : A Meshfree Particle Method. World Scientific, Singapore.

Lucy, L.B., 1977. A numerical approach to the testing of the fission hypothesis. Astron. J. (N. Y.) 82 (12), 1013–1024.

MATLAB, 2022. MATLAB 9.12.0.1927505 (R2022a). The MathWorks Inc., Natick, MA, USA.

Metzner, A.B., Feehs, R.H., Ramos, H.L., Otto, R.E., Tuthill, J.D., 1961. Agitation of viscous Newtonian and non-Newtonian fluids. Aiche J. 7 (1), 3–9.

Mohammed, A.M., Ariane, M., Alexiadis, A., 2021. Fluid-structure interaction in coronary stents: a discrete multiphysics approach. Chemengineering 5 (3), 60. Sep.

Mohammed, A.M., Ariane, M., Alexiadis, A., 2020. Using discrete multiphysics modelling to assess the effect of calcification on hemodynamic and mechanical deformation of aortic valve. ChemEngineering 4 (3), 48.

Morris, J.P., Fox, P.J., Zhu, Y., 1997. Modeling low Reynolds number incompressible flows using SPH. J. Comput. Phys. 136 (1), 214–226. Sep 1.

Pal, A., Abrahamsson, B., Schwizer, W., Hebbard, G.S., Brasseur, J.G., 2003. Application of a virtual stomach to evaluate gastric mixing and breakdown of solid food. Gastroenterology 124 (4), A673–A674. Apr.

Pazdniakou, A., Adler, P.M., 2012. Lattice Spring Models. Transp. Porous Media 93 (2), 243–262.

Pepin, X., Goetschy, M., Abrahmsen-Alami, S., 2022. Mechanistic models for USP2 dissolution apparatus, including fluid hydrodynamics and sedimentation. J. Pharm. Sci. 111 (1), 185–196. Jan.

Plimpton, S., 1995. Fast parallel algorithms for short-range molecular-dynamics. J. Comput. Phys. 117 (1), 1–19.

Prasanth, V.V., Jayaprakas, R., Mathew, S.T., 2012. Colon specific drug delivery systems: a review on various pharmaceutical approaches. J. Appl. Pharmaceutical Sci. 2, 163–169.

Sahputra, I.H., Alexiadis, A., Adams, M.J., 2020. A coarse grained model for viscoelastic solids in discrete multiphysics simulations. Chemengineering 4 (2), 30. Jun.

Sanfilipo, D., Bahman, G., Alexiadis, A., Garcia, A.Hernandez, 2021. Combined peridynamics and discrete multiphysics to study the effects of air voids and freeze-thaw on the mechanical properties of asphalt. Materials (Basel) 14 (1579), 1579.

Schütt, M., O'Farrell, C., Stamatopoulos, K., Hoad, C.L., Marciani, L., Sulaiman, S., Simmons, M.J.H., Batchelor, H.K., Alexiadis, A., 2022. Simulating the hydrodynamic conditions of the human ascending colon: a digital twin of the dynamic colon model. Pharmaceutics 14 (1), 184.

Schütt, M., Stamatopoulos, K., Batchelor, H.K., Simmons, M.J.H., Alexiadis, A., 2021. Modelling and simulation of the drug release from a solid dosage form in the human ascending colon: the influence of different motility patterns and fluid viscosities. Pharmaceutics 13 (6), 859.

Schütt, M., Stamatopoulos, K., Simmons, M.J.H., Batchelor, H.K., Alexiadis, A., 2020. Modelling and simulation of the hydrodynamics and mixing profiles in the human proximal colon using Discrete Multiphysics. Comput. Biol. Med. 121, 103819.

Stamatopoulos, K., 2022. Integrating Biopharmaceutics to Predict Oral Absorption Using PBPK Modelling. Biopharmaceutics. John Wiley & Sons Ltd, pp. 189–202.

Stamatopoulos, K., Batchelor, H.K., Alberini, F., Ramsay, J., Simmons, M.J.H., 2015. Understanding the impact of media viscosity on dissolution of a highly water soluble drug within a USP 2 mini vessel dissolution apparatus using an optical planar induced fluorescence (PLIF) method. Int. J. Pharm. 495 (1), 362–373. Nov 10.

Stukowski, A., 2010. Visualization and analysis of atomistic simulation data with OVITO-the Open Visualization Tool. Model. Simul. Mater. Sci. Eng. 18 (1), 015012.

Wang, B., Armenante, P.M., 2016. Experimental and computational determination of the hydrodynamics of mini vessel dissolution testing systems. Int. J. Pharm. 510 (1), 336–349. Aug 20.